RESEARCH ARTICLE

Volumetric-correlation PIV to measure particle concentration and velocity of microflows

Chuong Vinh Nguyen · Josie Carberry · Andreas Fouras

Abstract Volumetric-correlation particle image velocimetry (VPIV) is a new technique that provides a 3-dimensional 2-component velocity field from a single image plane. This single camera technique is simpler and cheaper to implement than multi-camera systems and has the capacity to measure time-varying flows. Additionally, this technique has significant advantages over other 3D PIV velocity measurement techniques, most notably in the capacity to measure highly seeded flows. Highly seeded flows, often unavoidable in industrial and biological flows, offer considerable advantages due to higher information density and better overall signal-to-noise ratio allowing for optimal spatial and temporal resolution. Here, we further develop VPIV adding the capability to measure concentration and increasing the robustness and accuracy of the technique. Particle concentrations are calculated using volumetric auto-correlations, and subsequently the velocities are calculated using volumetric cross-correlation corrected for variations in particle concentration. Along with the ability to calculate the particle concentration profile, our enhanced VPIV produces significant improvement in the accuracy of velocity measurements. Furthermore, this technique has been demonstrated to be insensitive to out-of-plane flows. The velocity measurement accuracy of the enhanced VPIV exceeds that of standard micro-PIV measurements, especially in near-wall regions. The 3D velocity and particle-concentration measurement capability of VPIV are demonstrated using both synthetic and experimental results.

1 Background

Particle image velocimetry (PIV) has been greatly extended to provide additional velocity components (from 2C to 3C), to more spatial dimensions (2D planar to 3D volume), and the ability to measure small flow scales (from macro to micro and nano). Initially, a PIV system consisted of a camera and a synchronized light sheet to capture a 2D2C velocity (Adrian 1991). The first extension to add the out-of-plane velocity component to an inherent planar velocity field was stereo PIV using 2 cameras by Arroyo and Greated (1991) and with 3 cameras by Fouras et al. (2008). Stereo PIV was again extended with multiple planes (Schroder and Kompenhans 2004; Kahler 2004) to obtain a full nine velocity gradient tensor. An optically complicated technique is Holographic PIV (Barnhart et al. 1994; Zhang et al. 1997) that allows a full 3D3C velocity field using 3D particle tracking velocimetry (PTV). Utilizing ray tracing to reconstruct a volume image from multiple cameras, Tomographic PIV (Elsinga et al. 2006) can provide a full 3D3C velocity field of a fluid volume, but requires multiple cameras, complicated calibration, high intensity laser, and some constraints on seeding density with respect to the number of cameras. One 3D3C technique relying on particle tracking is Defocusing PIV (Willert and Gharib 1992; Pereira et al. 2000; Pereira and Gharib 2002; Kajitani and Dabiri 2005; Grothe and Dabiri 2008) using a single lens mask with 3 holes, or alternatively 3 cameras with 3 lenses, forming a triangle to encode the depth

C. V. Nguyen
School of Physics and Monash Node of the CRC for Biomedical
Imaging Development, Monash University,
Melbourne, VIC 3800, Australia

J. Carberry
Department of Mechanical and Aerospace Engineering,
Monash University, Melbourne, VIC 3800, Australia

A. Fouras (✉)
Division of Biological Engineering, Monash University,
Melbourne, VIC 3800, Australia
e-mail: andreas.fouras@monash.edu

information as the distance between 3 images of the same particle. The lens mask with 3 pin holes allows 3D estimation of particle locations from a single camera but reduces both signal-to-noise ratio and viable levels of seeding density. Three separate cameras, however, can significantly improve the signal-to-noise ratio and raise the limit of seeding density for PTV-based techniques. As Defocusing PIV, like other PTV-based techniques, requires particle identification, it is limited to levels of seeding density where particle overlap is low enough for a high probability of particle identification. According to Adrian (2005), the highest seeding density achieved with PTV-based measurements was approximately 10^4 particles per image area of 1,024 × 1,024 pixels by Pereira and Gharib (2002).

Although fluorescent techniques for microscale biology flows have been used for decades in biological and medical studies (Tangelder et al. 1986), PIV was later extended to measure microflows by Meinhart et al. (2000) and has also been used to relate flow-induced shear to biological function (Nesbitt et al. 2009). PIV was further extended to the nanoscale by Yoda and Sadr (2004). Three-dimensional PIV techniques have also been extended to micro-PIV. Yoon and Kim (2006) and Pereira et al. (2007) applied defocusing concept to track 3D particle positions to produce 3D velocity fields of microflows. Park and Kihm (2006) proposed a 3D3C PTV technique based on the relation between particle depth position and the diameter of the outmost diffraction pattern ring. Scanning stereo micro-PIV was realized by Lindken et al. (2006) to produce a 3D3C velocity flow field of microchannel flow. Bown et al. (2006) further applied 3D particle tracking to stereo PIV images to obtain full 3D velocity measurements. Sheng et al. (2006) and Satake et al. (2006) developed inline micro holographic PIV to provide 3D velocity field using particle tracking. Limited space available in micro-PIV limits the viability of adding stereo cameras to improve spatial information and seeding density. Due to the increased diameter of out-of-focus particles in micro-PIV, particle overlap is more severe, placing greater restrictions on seeding density for PTV-based methods. The seeding density of defocusing micro-PIV obtained (Yoon and Kim 2006; Pereira et al. 2007) was approximately 10^2–1.5×10^3 particles per image area of 1,024 × 1,024 pixels. Furthermore, due to small numerical apertures defocusing require high intensity illumination which can exceed the damage threshold of biological flows.

While most 3D PIV techniques rely on spatial image data from multiple cameras, little work has been done to extract the out-of-plane velocity information buried inside the cross-correlation. The cross-correlation contains information from throughout the depth of the image and can be considered as the probability distribution function (PDF) of velocity. Cummings (2000) proposed an optimal filter to improve velocity measurement. By using a second-order velocity model in an optimal filter, he was able to obtain both mean velocity and velocity gradients. To obtain volume flow rate alone, Plecis et al. (2008) proposed integrating the cross-correlation in the flow direction. Fouras et al. (2007) were able to produce a 3D velocity field within a cylindrical tube using X-rays as the light source that produces no out-of-focus particles. While these techniques ignore or minimize the out-of-focus effect in volume illumination, this effect can be utilized to extract out-of-plane velocity information. Erkan et al. (2008) proposed a 3-component velocity measurement technique where the out-of-plane component is calculated from the change the cross-correlation intensity gradient. However, this technique is limited to producing measurements on the focal plane that cuts across the channel at an angle. The only PIV technique that truly utilizes out-of-focus effects for 3D volume velocity measurements is volumetric-correlation PIV or VPIV (Fouras et al. 2009). An advantage of this method is that as a correlation-based method, it can be applied to microscale flows with much higher seeding density than 3D PTV-based methods requiring particle identification. In theory, the only limit on seeding density for correlation-based methods is image saturation.

2 Introduction to out-of-focus effect and volumetric-correlation PIV

Out-of-focus effects are a prominent phenomenon in micro-PIV where the whole flow is illuminated and images of particles throughout the depth are captured onto the same image. Particles at different z (depth) locations appear differently in the image; if the particle image is approximated as a Gaussian distribution then, as described by Olsen and Adrian (2000), the particle image diameter d_e and intensity $I(r, z)$ from a particle at a given z location can be expressed as:

$$d_e^2 = M^2 d_p^2 + 5.95(M + 1)^2 + \lambda^2 f^{\#2} + \frac{M^2 z^2 D_a^2}{(s_0 + z)^2} \tag{1}$$
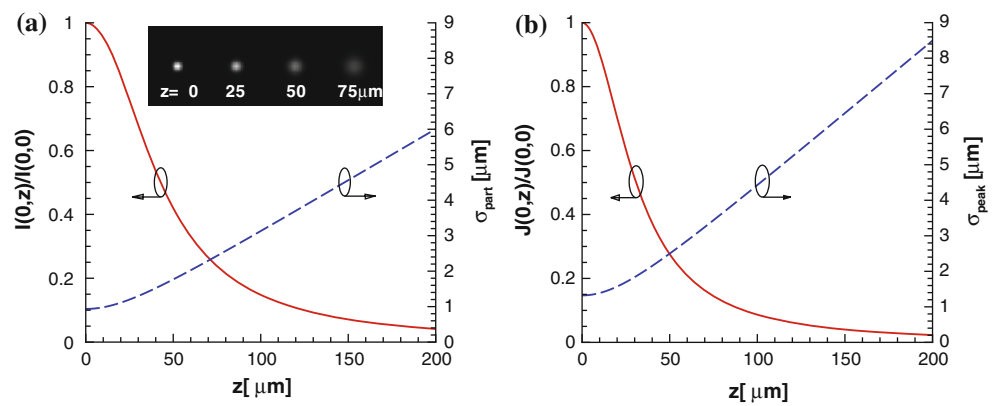
$$I(r, z) = I_0 \exp\left(\frac{-4\beta^2 r^2}{d_e^2}\right) \tag{2}$$

with

$$I_0 = \frac{J_p D_a^2 \beta^2}{4\pi d_e^2 (s_0 + z)^2} \tag{3}$$

where d_p is the particle real diameter, M the lens magnification, $f^{\#}$ the lens focal number, D_a the lens aperture diameter, s_0 the lens working distance, λ the wavelength of light emitted from the particle, J_p the flux of the light and $\beta = 3.67$ (Adrian and Yao 1985).

Fig. 1 Out-of-focus effect on **a** the particles image intensity I, and half width σ_{part}, and **b** the intensity J and half width σ_{peak} of the auto-correlation peak of the particles (3 μm particle and lens of $M = 5$, NA = 0.12). Intensity (*solid curve*) and half widths (*dashed curve*) are shown as functions of the distance from the focal plane (z). The *inset* in figure **a** shows the variation of a particle image with increasing out-of-focus

The effect of distance from the focal plane, or the out-of-focus effect, on a particle's image intensity and half width $\sigma_{part} = \frac{d_e}{2\sqrt{2\beta}}$ is shown in Fig. 1a. This figure is obtained using Eqs. 1, 2, and 3 for an objective lens of magnification $M = 5$, numerical aperture NA = 0.12 and working distance $s_0 = 14$ mm with particle diameter $d_p = 3$ μm. The corresponding variations of the particles auto-correlation intensity and half width σ_{peak} with distance (z) from the focal plane are shown in Fig. 1b. With the exception of the region immediately adjacent to the focal plane, the particle size represented by σ_{part} increases linearly with z, as does the auto-correlation σ_{peak}.

In micro-PIV, the cross-correlation contains signals from both in-focus and out-of-focus particles. Correlation signals from out-of-focus particles cause measurement bias. A classical example of this bias is in microchannel flows, where significant error occurring in near-wall regions and in the flow center (Nguyen et al. 2010). This bias error has been considered as a major problem (Meinhart et al. 2000; Olsen and Adrian 2000), and several measurement techniques have been developed to reduce the effect of out-of-focus particles (Bitsch et al. 2005; Gui et al. 2002; Bourdon et al. 2004; Nguyen et al. 2010). However, in volumetric-correlation PIV (VPIV) (Fouras et al. 2009), the out-of-focus effect is in fact the key element that allows the measurement of velocity profile in the z direction from a single correlation peak. This method is based on the proposition that the cross-correlation Cx_{full} of an image pair containing particles distributed in the z direction is linearly proportional to the summation of the cross-correlations $Cx_{2D}(\delta x, \delta y, z)$ of the particles at individual z positions:

$$Cx_{full} = a \sum_{z=z_1}^{z_N} Cx_{2D}(\delta x, \delta y, z) + b \tag{4}$$

where a and b are constants, and $Cx_{2D}(\delta x, \delta y, z)$ the cross-correlation function with the displacement components δx and δy of particles located at z, and $z_1 \ldots z_N$ the depth range of particles within the flow.

The cross-correlation $Cx_{2D}(\delta x, \delta y, z)$ can be expressed as a Gaussian function:

$$Cx_{2D}(\delta x, \delta y, z) = J(0, z) \exp\left(-\frac{(\hat{x} - \delta x)^2 + (\hat{y} - \delta y)^2}{2\sigma_{peak}(z)}\right) \tag{5}$$

where $J(0,z)$ is the correlation peak intensity ($r = 0$) of a particle at location z, $\hat{x}$ and $\hat{y}$ are horizontal and vertical coordinates in the correlation map.

In VPIV, the auto-correlations of particles are used as calibration data to produce $J(0,z)$ and $\sigma_{peak}(z)$. Calibration images are captured by scanning a thin layer of seeding particles in the z direction. Gaussian fitting is performed on the auto-correlations of the calibration images to obtain $J(0,z)$ and $\sigma_{peak}(z)$ to allow fast generation of $Cx_{2D}(\delta x, \delta y, z)$ using Eq. 5.

The principle of the VPIV measurement technique is illustrated in Fig. 2. Unlike standard PIV, to measure velocity in VPIV, the channel is positioned at a distance z_0 from the focal plane of the camera lens, as shown in Fig. 2a. This setting not only produces unique values of correlation intensity $J(0,z)$ and half-width σ_{peak} in the z direction but also avoids the nonlinear part of σ_{peak} and the peak of $J(0,z)$ to improve optimization speed and accuracy (Fouras et al. 2009). The channel depth H must be small enough to avoid the region of low signal-to-noise ratio at a higher z value due to low correlation intensity and variation. In the case presented in this paper, the channel depth was approximately 2/3 of the depth of correlation of the optical system. Figure 2a also defines the coordinate system with the origin located on the focal plane and the z-axis as the out-of-plane direction. In addition, using larger than normal maximum particle displacements between 2 image exposures improves the optimization accuracy. This is especially true when measuring complicated velocity profiles, as larger displacement generates wider volumetric cross-correlation peaks and more velocity information. However, the maximum displacement is limited by Brownian motion
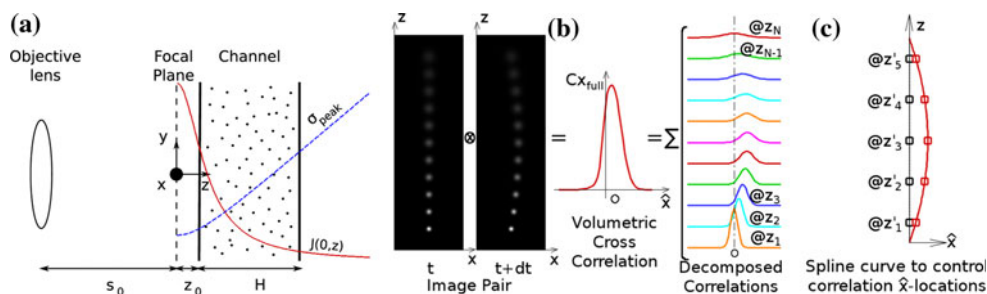
Fig. 2 Illustration of volumetric-correlation PIV principle (Fouras et al. 2009). **a** Schematic diagram including coordinate system for VPIV measurements (Fouras et al. 2009). The focal plane is at a working distance s_0 from the objective lens and at distance z_0 from the channel to avoid the nonlinear part of σ_{peak}. The channel height H is chosen small enough to cover a region of strong correlation intensity for sufficient signal-to-noise ratio. The origin of the coordinates is at the focal plane. The principal flow direction is the x direction. **b** The correlation of an image pair of particles distributed over the channel depth z yields a full volumetric-correlation peak. This peak can be considered as the sum of the correlations of all particles at different z locations. To obtain the velocity profile, the volumetric-correlation peak is decomposed into correlation peaks at (@) evenly spaced z positions such that their sum is equal to the given volumetric cross-correlation. **c** Spline interpolation used to control horizontal locations of decomposed correlations at z_1 to z_N to reduce the degree of freedom. The spline curve is the measured velocity profile when the optimization converges. Five nodes from z'_1 to z'_5 may be used here, however, more or less nodes are needed for more general velocity profiles

(hence the time interval), in-plane velocity gradients and image window size. Finally, ensemble-averaged correlation (or correlation averaging) with sufficiently large interrogation windows produce a high-definition volumetric cross-correlation peak containing velocity information at all z positions.

The velocity measurement in VPIV is performed by decomposing Cx_{full} into $Cx_{2D}(\delta x, \delta y, z)$ at different z locations. The left of the Fig. 2b shows two successive synthetic images of particles located at various z positions across the channel depth with the focal plane located outside the channel. The cross-correlation of the image pair containing all theses particles yields a volumetric-correlation function/peak shown in the middle of the figure. To measure velocity profile in z direction, the volumetric-correlation peak needs to be decomposed into cross-correlations at evenly spaced z locations, as shown on the right of Fig. 2b. The horizontal locations of the decomposed peaks give the displacement components δx throughout the depth (similarly for δy). The correlation decomposition is performed using a nonlinear least-squares solver (Levenberg–Marquardt algorithm) that fits the full correlation peak to the sum of the auto-correlation peaks of N particles equally spaced in the z direction. For a flow depth of 100 μm, $N = 100$ was found to be sufficient. To reduce the number of degrees of freedom in the velocity component and allow the solver to provide a stable solution, a curve fitting (piece-wise linear or spline) is used to control the displacements of the correlation peaks as shown in Fig. 2c. The displacements at the nodes are directly optimized by the solver. In this illustration, a simple parabolic velocity profile can approximated by a 5-node spline. More or fewer nodes may be required for other velocity profiles. The nodes can be additionally adjusted to be either evenly or unevenly spaced to fit better with different profiles. One interrogation window can provide a velocity profile in the depth direction, and by combining the measurements from several interrogation windows, a 3-dimensional 2-component (3D2C) velocity field can be achieved from an image region.

Due to the use of ensemble-averaged correlation and spline interpolation, VPIV measurements are currently restricted to steady flows without abrupt spatial velocity variations. Fortunately, most microscale flows are laminar and fall into this category.

Our previous study (Fouras et al. 2009) showed that VPIV can provide accurate velocity measurements with synthetic image data of a range of flow fields with seeding concentration from 10^6 to 10^{10} particles/ml. However, a reduced measurement accuracy was obtained with experimental image data. The reason for the accuracy degradation in the experimental data has been identified as the variation of particle concentration across the channel depth. Typically, maximum particle concentration occurs at 0.6 channel radii from the center with very low concentrations near the walls (Cao and Wereley 2006). The effect of concentration variation within the channel depth was not considered by Fouras et al. (2009) and constant particle concentration was used in all synthetic image generation. As a result, the VPIV measurements produce signification errors when inappropriately applying constant particle concentration assumption to real flows.

Figure 3 shows the measurement result obtained from 2 sets of synthetic image data of (a) constant concentration and (b) varying concentration consistent with real channel flow. The total measurement error across the flow field is represented by l^2_{norm} where:
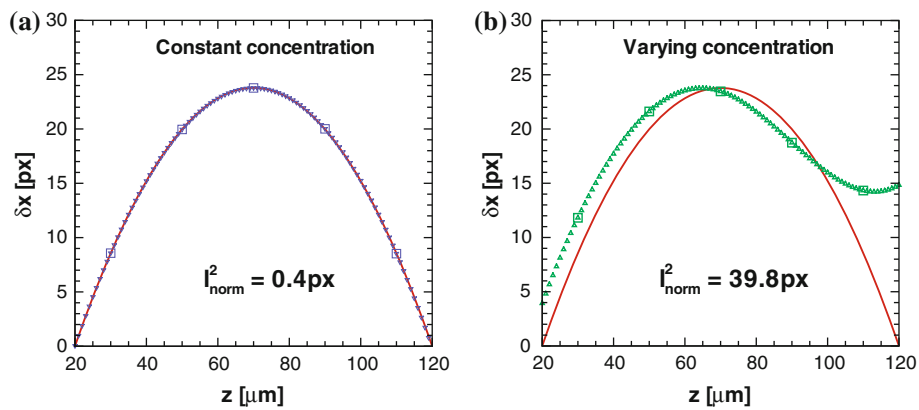
Fig. 3 VPIV velocity measurements of synthetic parabolic flows with **a** constant concentration of tracer particles and **b** varying concentration (Eq. 7). The *solid curve* is the exact velocity profile. The *gradient symbols* are the measurement data points from a flow with constant concentration, and *delta symbols* are for the measurement data points from a flow with constant concentration. Original VPIV (Fouras et al. 2009) yields accurate measurement in the first case while giving poor measurement in the second case

$$l^2_{norm} = \sqrt{\sum_{z=z_0}^{z_0+H}(\delta x_{exact}(z) - \delta x_{meas}(z))^2} \qquad (6)$$

To allow comparison between different experiments l^2_{norm} is calculated using z increments of 1 μm in this paper.

The measurement accuracy is excellent when the concentration is constant, but quite poor when the concentration varies. To improve VPIV measurement accuracy with real flows of varying particle concentrations, it is necessary to extend VPIV to include the effect of particle concentration. This in turn requires the concentration information. In this paper, we propose an enhanced VPIV technique that includes a novel concentration measurement technique yielding improved accuracy in the velocity measurement accuracy.

3 Enhanced volumetric-correlation PIV with particle concentration

To measure particle concentration $C_{part}(z)$, a method similar to velocity measurement in VPIV is proposed. Our study confirmed the finding by Keane and Adrian (1992) that the magnitude of cross- and auto-correlations is linearly proportional to particle concentration. For a particle concentration given by following equation:

$$C_{part}(z) = \sin\frac{(z-z_0)\pi}{H} + \frac{1}{3}\sin\frac{3(z-z_0)\pi}{H}, \qquad (7)$$
$$\text{for } 0 \le z - z_0 \le H$$

the effect of the varying particle concentration $C_{part}(z)$ on the effective correlation peak intensity $J'(0,z)$ is shown in Fig. 4. For comparison, the correlation intensity for constant particle concentration $J(0,z)$ is also shown. With varying concentration $C_{part}(z)$ shown by the solid curve, the
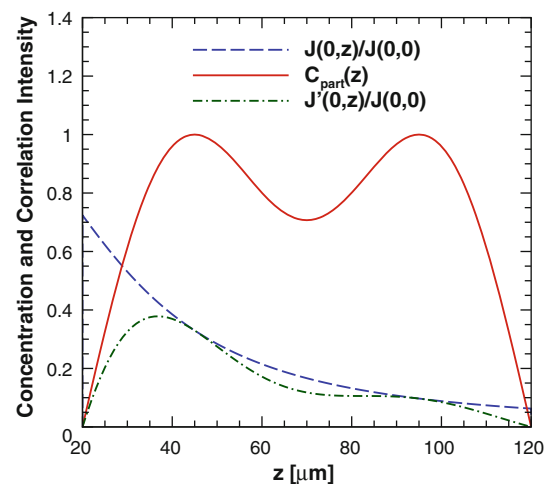

Fig. 4 Effect of particle concentration on the mean intensity of the auto-correlation peak within a channel of 100 μm depth with the focal plane located at $z = 0$. For constant concentration, the correlation intensity $J(0,z)$ is as shown by the *dash-dash curve*. However, with a varying particle concentration $C_{part}(z)$ (*solid curve*), the effective correlation intensity $J'(0,z)$ shown as *dashed-dot* is equal to $C_{part}(z) \times J(0,z)$

effective correlation intensity $J'(0,z)$ shown by dash-dot curve is equal to $C_{part}(z) \times J(0,z)$.

To incorporate variations in concentration the volumetric cross-correlation in Eq. 4 is now rewritten as:

$$Cx_{full} = a\sum_{z=z_1}^{z_N} C_{part}(z) \times Cx_{2D}(\delta x, \delta y, z) + b \qquad (8)$$

Before calculating displacement components δx and δy, particle concentration $C_{part}(z)$ has to be obtained. Fortunately, the concentration can be obtained from the full auto-correlation Co_{full} using the same methodology as used for velocity. Thus, Co_{full} can be expressed as:

$$Co_{full} = a \sum_{z=z_1}^{z_N} C_{part}(z) \times Co_{2D}(z) + b \qquad (9)$$

where $Co_{2D}(z)$ is the auto-correlation of calibration images at different z locations and $Co_{2D}(z)$ can be generated quickly at an arbitrary z location using $J(0,z)$ and $\sigma_{peak}(z)$:

$$Co_{2D}(z) = J(0,z) \exp\left(-\frac{\hat{x}^2 + \hat{y}^2}{2\sigma_{peak}(z)}\right) \qquad (10)$$

Using a similar least-squares solver with spline interpolation, $C_{part}(z)$ can be calculated from Eq. 9 as illustrated in Fig. 5. The location of the channel walls can also be located as corresponding to the outer bound of the particle distribution, z_1 & z_n. This simplifies the experimental procedure as there is no need to accurately locate the wall locations before taking measurements. After obtaining $C_{part}(z)$, the displacement profile is obtained by solving Eq. 8, yielding the 2-component velocity profile in the z direction. Additional velocity measurements on an x–y grid gives a 3D-2C velocity field.

In addition, the cross-correlation peak can be used to improve the accuracy of concentration measurement if a good estimation of velocity is known. Thus, a multi-pass scheme can be used to obtain concentration and velocity profiles with increasing accuracy. For example, first concentration is obtained from the auto-correlation and velocity is then calculated from the concentration and the cross-correlation. This velocity is then used to re-calculate the concentration using the cross-correlation following Eq. 4.

The calibration auto-correlations are used directly without fitting to compensate for errors associated with optical aberration and non-Gaussian particle intensity

profiles. By directly using the calibration auto-correlations, the VPIV technique can also be applied to particles with diffraction rings captured with high magnification and high numerical lenses. $Co_{2D}(z)$ and $Cx_{2D}(\delta x, \delta y, z)$ at any z location are generated by 3D interpolation from the stack of calibration auto-correlations, instead of using Eqs. 5 and 10. To speedup the interpolation process, $Co_{2D}(z)$ is obtained using 1D interpolation in the z direction from the stack of calibration auto-correlations, then $Cx_{2D}(\delta x, \delta y, z)$ is obtained from $Co_{2D}(z)$ using 2D-interpolation on the $\hat{x} - \hat{y}$ plane. When the size of out-of-plane particles approaches that of the PIV interrogation window, the size of the window, which can be considered as a filtering kernel, can affect the correlation signal. As a result, the same window size should be used to compute calibration auto-correlations and volumetric (auto- and cross-) correlations.

Calibration also takes into account inhomogeneous particle size by producing a statistical representation. In fact, variations in particle diameter have minimal effect on the actual size of out-of-focus particle images. As shown in Eq. 1, as z becomes sufficiently large, the contribution of particle diameter d_p becomes less significant and the effective diameter d_e of the particle image becomes a linear function of z. Spatially inhomogeneous illumination and spatial distortion in particle location in the x–y plane (Yoon and Kim 2006) can be corrected by calibration and can also be minimized by keeping the particle displacement between successive exposures relatively small.

Depending on the temperature and scale of the flow as well as the size of the particles, Brownian motion may affect PIV measurements (Santiago et al. 1998; Olsen and Adrian 2000). Chamarthy et al. (2009) showed that for submicron particles, the width of the cross-correlation peak is
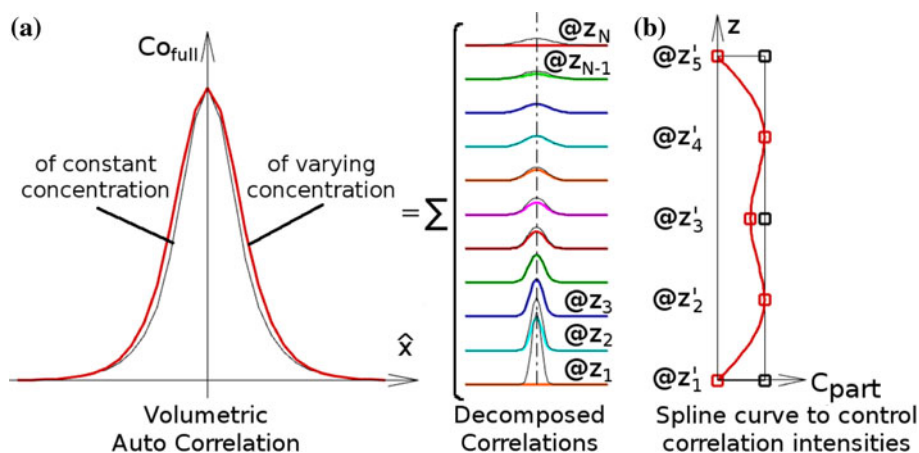

Fig. 5 Least-square solution of the particle concentration profile. **a** The auto-correlation peak (*thick solid curve*) on the *left* gives the concentration profile in terms of the superimposed variation of correlation intensities at different z locations. **b** To reduce the number of variables to be optimized, a spline interpolation is used. The

constant concentration (*thin straight line*) can be provided as initial guess at the start of the fitting process. The corresponding initial Gaussian peaks and volumetric-correlation peak are shown as *thin black curves*. The *thick solid curves* are shown as the final result when the fitting converges

a function of temperature. However, in many cases, Brownian motion is negligible. Following Chamarthy et al. (2009), the mean square of Brownian motion $\langle \Delta s_{BM}^2 \rangle$ between the two image exposures of 2 ms interval was estimated to be 3.25×10^{-4} μm^2 for 3 μm particles in 20°C glycerol solution (20% weight). This is too small to have any detectable effect on the cross-correlation peak, hence the auto-correlation peak can be used for the calibration. In addition, $s_{o,c}^2 = s_{o,a}^2 + 8M^2\langle \Delta s_{BM}^2 \rangle$, where $s_{o,c}^2$ and $s_{o,a}^2$ are the peaks with and without Brownian motion (Chamarthy et al. 2009). Therefore, if the focal plane is farther from the channel wall, $s_{o,a}^2$ becomes larger and the Brownian motion becomes less significant. In the case that Brownian motion can not be ignored, it can be corrected for by using the cross-correlation peaks obtained from the calibration image pairs of zero-velocity. Such calibration image pairs should be taken from the particle spread having the same temperature and time delay between exposures as those for the flow to be measured.

In fact, PIV correlations are affected by not only particle concentration but also out-of-plane motion (Olsen and Bourdon 2003), time-varying motion (Poelma and Westerweel 2010), and in-plane gradients (Keane and Adrian 1992; Huang et al. 1993). Although these factors are not corrected for in the work presented in this paper, their effects are quantified in Sect. 4.2.

4 Validation by numerical experiments

To validate the measurement performance of VPIV, synthetic images were generated using known concentration and velocity profiles in the depth direction. For comparison, measurements of concentration and velocity were also performed using scanning PIV techniques.

4.1 Concentration and velocity measurements using scanning PIV techniques

Concentration in the depth direction is obtained by image filtering, thresholding, and particle counting. As needed and at each scanning position, only particle counting is necessary. High-pass filtering was applied to remove out-of-focus particles. For velocity measurement, both correlation averaging and image overlapping were used and compared. Correlation averaging (Meinhart et al. 2000) has been a gold standard method for micro-PIV measurements and is usually combined with image filtering (Gui et al. 2002) and thresholding (Zheng and Silber-Li 2008) to provide good measurement accuracy. Image overlapping (Wereley et al. 2002) is a method that artificially increases the seeding density in micro-PIV images providing

improved velocity measurement accuracy (Nguyen et al. 2010) by reducing the depth of correlation.

The study was performed in a 100-μm-deep channel using 3 lenses: $M = 5$ and NA $= 0.15$; $M = 10$ and NA $= 0.20$; and $M = 20$ and NA $= 0.40$. Synthetic images were generated from a parabolic velocity profile in the z direction and an average concentration of 44,444 particles/mm^3 (corresponding to 10,000 particles/image for a lens with $M = 5$). Particles of 3 μm diameter are randomly distributed with uniform probability over x & y and non-uniform probability in z. At each of 21 scanning positions, 100 image pairs of $1,024 \times 1,024$ pixel size were generated for concentration and velocity measurements. The concentration profile in the z direction is given by Eq. 7.

Figure 6 shows the concentration measurements obtained using scanning. The measurements were normalized by the area underneath the curves and error bars give the standard deviation of the measurements. The accuracy of the measurement increases with increasing numerical aperture as long as there are sufficient particles inside the depth of correlation. Good measurement can be obtained with NA $= 0.40$.

Figure 7 shows the velocity measurements obtained using correlation averaging and image overlapping. For easy comparison between the measurements using different lenses, the same maximum pixel displacement of the flow was maintained. Image overlapping performs significantly better than correlation averaging, reducing the l_{norm}^2 error approximately 50–60%. As expected, the higher numerical
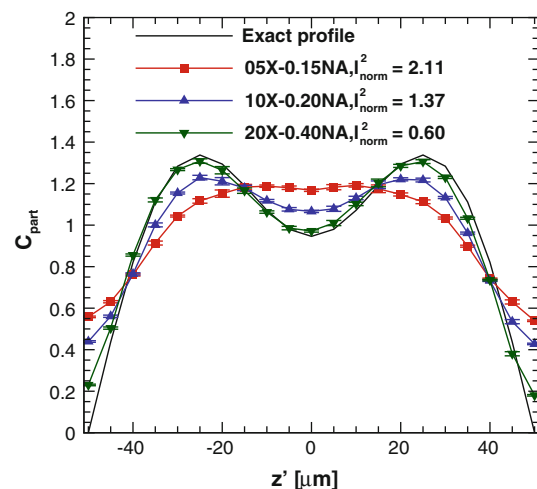

Fig. 6 Concentration measurements obtained from synthetic scanning PIV images using image filtering and particle counting. *Solid curves without symbols* represent the exact profiles. *Symbols with error bars* represent the measurement points. Here $z' = zz_0H/2$. The l_{norm}^2 values represent the total measurement errors across the measurement volume. The measured concentration versus exact concentration follows Eq. 7. Error in concentration measurement decreases as lens numerical aperture increases
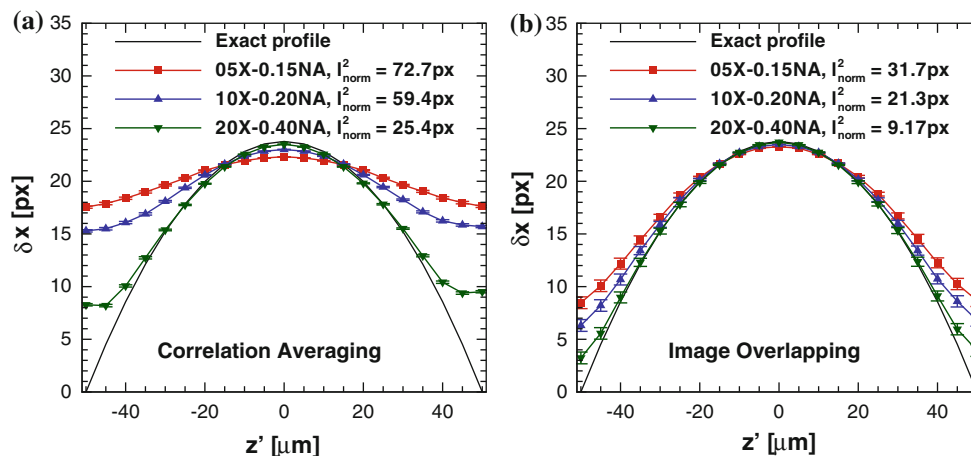
(a) Correlation Averaging — Exact profile; 05X-0.15NA, l^2_{norm} = 72.7px; 10X-0.20NA, l^2_{norm} = 59.4px; 20X-0.40NA, l^2_{norm} = 25.4px

(b) Image Overlapping — Exact profile; 05X-0.15NA, l^2_{norm} = 31.7px; 10X-0.20NA, l^2_{norm} = 21.3px; 20X-0.40NA, l^2_{norm} = 9.17px

Fig. 7 Velocity measurements obtained from synthetic scanning PIV images using **a** correlation averaging and **b** image overlapping. *Solid curves without symbols* represent the exact profiles. *Symbol with error bars* represent the measurement points. The l^2_{norm} values represent the total measurement errors across the measurement volume. Error velocity measurement decreases as lens numerical aperture and magnification increase. As compared with correlation averaging, image overlapping provides more accurate velocity measurements

aperture of 0.40 produces the most accurate results, however, velocities at the wall are significantly overestimated.

4.2 Concentration and velocity measurements using VPIV

To validate the enhanced VPIV algorithm, 2 sets of 2,048 synthetic image pairs of 1,024 × 1,024 8-bit pixels are generated for 2 microchannel flows. No noise is added into the images. The optical set-up for synthetic image generation is shown in Fig. 2a with H = 100 μm. The image formation uses a lens of magnification M = 5, numerical aperture NA = 0.12, working distance s_0 = 14 mm, with the focal plane located 20 μm outside the channel at z' = −70 μm. The flow has a parabolic velocity profile in x direction. Particles, 3 μm in diameter are randomly distributed with uniform probability over x & y and nonuniform probability in z. Two different particle distributions were studied: in the first case, the particle concentration in z is controlled by Eq. 7 and occupies the whole channel depth; in the second case, the particle concentration was chosen to be nearly constant in the center following this equation:

$$C_{part}(z') = \left[1 - \exp\left(-\frac{z'-R}{0.2R}\right)\right]\left[1 - \exp\left(-\frac{R-z'}{0.2R}\right)\right],$$
$$\text{for } -R \leq z' \leq R \tag{11}$$

The second case (case 2A) also has a nonsymmetric velocity profile with a region of reverse flow similar to that behind back-facing step. Additional flow conditions are further superimposed to case 2A to validate the VPIV method in the presence of out-of-plane velocities (cases 2B and 2C), in-plane velocity gradients (cases 2D and 2E), or time-varying velocity (cases 2F and 2G). These flow conditions are used to show that VPIV is robust and applicable to velocity profiles found in real flows.

The concentration profiles are measured using the enhanced VPIV method with results shown as dashed curves in Fig. 8a–b along side the exact concentrations as solid curves. The concentration measurements also provide the region containing particles corresponding with the channel depth in both cases with accuracy greater than 1 μm. For the first case (concentration profile shown in Fig. 8a), there is a very good agreement between the measured and the exact concentrations. VPIV provides a measure accuracy better than that of the best scanning PIV measurement using the NA = 0.40 lens. For the second case (concentration profile as shown in Fig. 8b), the concentration accuracy is comparable with the best accuracy provided by scanning. In both cases, the VPIV concentration measurements oscillates around the true profile. This is due to the limited concentration information contained in the correlations and the oscillatory nature of spline interpolation.

Finally, the velocity profiles are obtained using the two measured concentrations. For comparison, velocities are also measured using an assumption of constant concentration as if no information of particle concentration is available. The results are shown in Fig. 8c–f. Using a constant concentration, Fig. 8c–d, the measured velocity profiles are shifted and distorted at the far end of the profile. Using the measured concentrations, Fig. 8e–f, the measurements yield very good agreement with the exact velocity profiles. Using the measured concentration drastically reduces the measurement errors. The l^2_{norm} of the error for the two cases is reduced by 96 and 91%, respectively, compared with the result using the constant concentration assumption. Compared with the errors
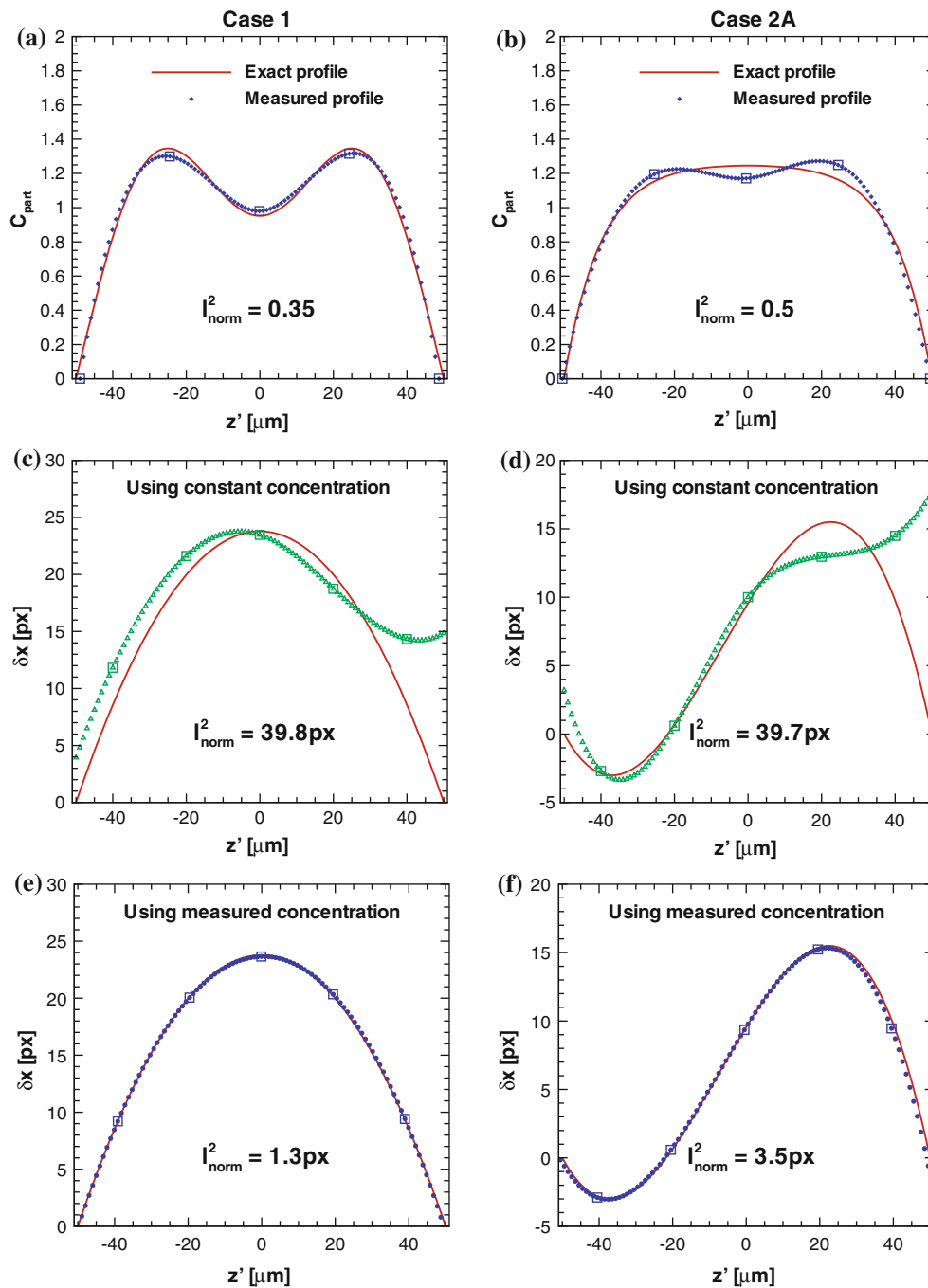
Fig. 8 Concentration and velocity measurements obtained by VPIV shown on the *left* and the *right columns* for two types of concentrations. Two sets of 2,048 synthetic images were generated from channel flows of 100 µm depth seeded with 3 µm particles and lens of 5 × magnification and numerical aperture of 0.12. Here $z' = z - z_0 - H/2$. *Solid curves* represent the exact profiles. *Dots* represent the measurement points (concentration or velocity) and *squares* the nodes of the spline interpolation for the measurements. **a** Measured concentration versus the exact concentration which follows Eq. 7. **b** Measured concentration versus exact concentration which follows Eq. 11. *Solid curves* represent the exact concentrations. *Squares* represent the nodes for the spline solution, or the measurements, which are shown as *dashed curves*. **c**, **d** Velocity profiles measured using a uniform concentration assumption. **e**, **f** Velocity profiles measured using the measured concentration profile. The l^2_{norm} values represent the total measurement errors across the measurement volume. There is an enormous reduction in errors (97 and 91%, respectively) between the measurements using constant concentration assumption (**c** and **d**) and the ones using the measured concentrations (**e** and **f**), respectively.
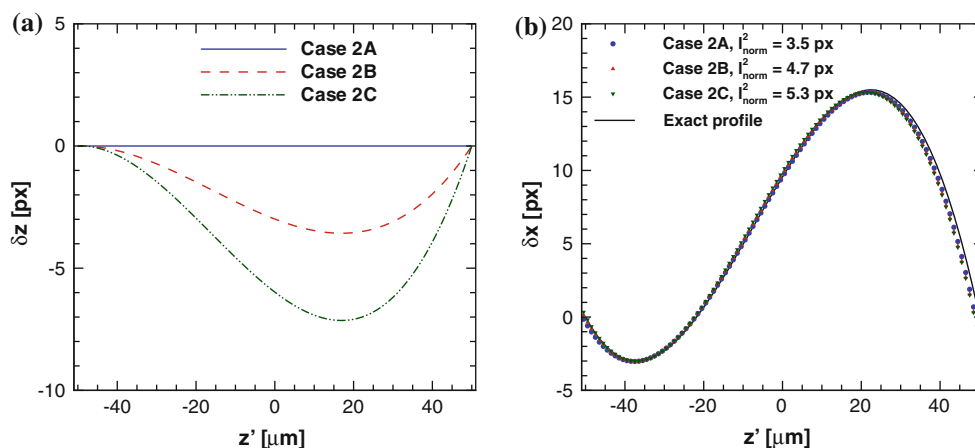
(a)

(b)

Fig. 9 The effects of out-of-plane velocity component to the velocity measurement accuracy. **a** Increasing out-of-plane velocities where case 2A has zero magnitude and case 2B has half of the magnitude as compared with that of case 2C. The out-of-plane displacement is

shown in pixel unit where one pixel is equivalent to 1.472 μm. **b** Corresponding measured velocities and l^2_{norm} with respect to the exact velocity profile

obtained using the best scanning results (by image overlapping with NA = 0.40 lens), there is a reduction of 86 and 62% in the error for the two cases. In addition, VPIV requires the same or less total number of image pairs and a lens of much lower NA than that of scanning PIV.

The effect of out-of-plane motion on the velocity measurement accuracy is shown in Fig. 9a–b. The measurement accuracy is shown to be insensitive to out-of-plane motion. With an out-of-plane velocity of 50% of the in-plane component, the measurement error is only 6.5% of the in-plane component.

The effect of the in-plane velocity gradient (du/dy) on the measurement accuracy is shown in Fig. 10. By increasing in-plane velocity gradient from 0 to 0.01, the

velocity measurement degrades significantly, especially in the near-wall region. This is due to the large image window that results in a maximum 2.5 pixel difference from one side to the opposite side for case 2D. As always in PIV for improving the measurement accuracy, window sizes need to be optimized to minimize the effect of the gradient.

The effect of time-varying in-plane velocity on the measurement accuracy is shown in Fig. 11. With an increasing velocity variation, the deviation of the velocity measurement from the true profile increases. However, the measurement accuracy is not significantly affected by the linear time-varying velocity. For case 2F, the velocity ranges from 90 → 110% of the velocity in case 2A over the
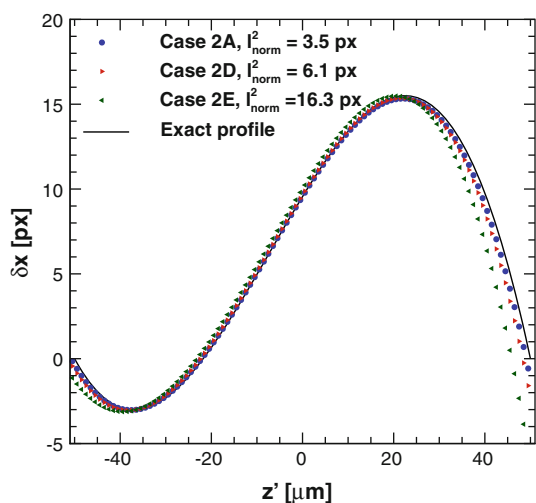

Fig. 10 The effect of in-plane velocity gradient (du/dy) on the velocity measurement accuracy. The gradient in cases 2A, 2D, and 2E corresponds to 0.0, 0.005, and 0.01 pixel/pixel, respectively.
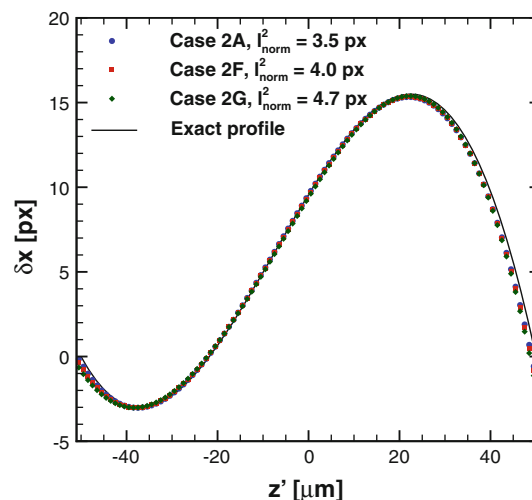

Fig. 11 The effect of time-varying in-plane velocity on the velocity measurement accuracy. The velocity is constant in time in case 2A. In case 2F, the velocity varies linearly within the time interval from 90 to 110% of the exact velocity in case 2A. In case 2G, the velocity range is from 85 to 115%

recording time of the image set. For case 2G, the velocity range is $85 \rightarrow 115\%$ and the measurement error is within 10% of the in-plane component.

In summary, VPIV can provide comparable concentration measurement accuracy and significantly better velocity measurement accuracy without scanning and therefore using lower-quality or cheaper hardware than scanning PIV.

5 Validation by laboratory experiments

To confirm the capability of VPIV with real image data, laboratory experiments were performed. Again both scanning PIV and VPIV measurements were performed on the same channel flows using similar optical settings to those used in the numerical experiments. The volume was illuminated by a green dual-head pulse laser (Continuum Inc. Minilite PIV) running under low-intensity mode. Fluorescent particles of 3 µm diameter (Duke Scientific Co red polystyrene microspheres) were seeded at a concentration of 7.1×10^7 particles/ml (or 2.8×10^4 particles per $1,024 \times 1,024$ pixel area). The experiment was not designed to test for the highest possible seeding density and higher seeding density is possible. The working fluid was 20% (by weight) glycerol solution prepared to match with the particle density of 1.05 g/cm^3. The certified standard deviation of the particle size was 1.1%. The mean square of the particle Brownian motion was estimated at 3.25×10^{-4} µm^2 which is negligible compared with the particle diameter. The solution was dispersed in ultrasonic bath to reduce particle clumps, which can be a significant source of error. Constant flow was produced by a syringe pump (Harvard PHD 2000) using a glass 5 cc syringe (Popper and Sons). The flow rate was maintained at 0.05 ml/min through a nominal 0.1×1 mm channel (VitroCom vitrotube) with the maximum velocity approximately 11.8 mm/s. The channel depth was measured to be approximately 105 µm at the channel center. The channel was aligned to the horizontal direction of the images. The refractive index of the glycerol solution was estimated at 1.36, making the channel height appear as 77.2 µm. The Reynolds number based on maximum velocity and channel height was 0.86. PIV images, $1,024 \times 1,024$ pixels in size, were captured using a PCO 4000 camera.

5.1 Concentration and velocity measurements by scanning PIV

Scanning PIV was performed using a lens (Leica) of $M = 20$ and NA $= 0.40$. There were 15 scanning positions within the channel depth. At each position, 300 image pairs were obtained. The images were band-pass filtered following (Nguyen et al. 2010) to remove particle clumps before counting particles for concentration measurement, or applying correlation averaging or image overlapping for velocity measurement. To reduce error due to background noise, only particles of more than 5 pixels size were counted for the concentration measurement. For velocity measurements, image templates of 129×129 pixels with 50% area overlapping and 10 pixel shifting in the flow direction were used for PIV correlations.

Concentration and velocity measurements produced by scanning PIV are shown in Fig. 13a and c, respectively. Concentration is quite noisy and nonzero at the walls. Velocity measurements at the channel center obtained with correlation averaging and image overlapping are compared with the theoretical velocity profile. As expected, image overlapping performs better in the near-wall region than correlation averaging, even though the accuracy of correlation averaging is significantly improved by image filtering. However, both methods significantly overestimate the near-wall velocities and slightly underestimate center-line velocities.

5.2 Concentration and velocity measurements by VPIV

The VPIV measurement were taken using $M = 5$ and NA $= 0.15$ (Leica) lens, yielding an image resolution of 1.8 µm/px. The focal plane was located at approximately 40 µm outside the lower wall of the channel. A 2 ms delay between successive exposures gave a maximum particle displacement of approximately 16 pixels. The experimental images contained particle clumps and significant dark-current noise, not present in the synthetic images, which significantly affected the shape of the volumetric-
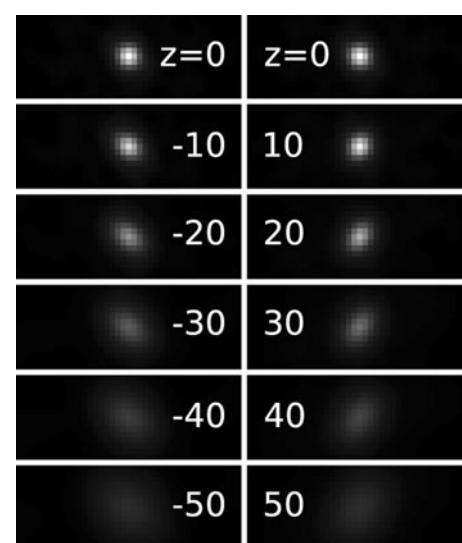

Fig. 12 Calibration auto-correlation peaks show the variations of radial optical aberration with particle position in the z direction

correlation peaks. As image filtering distorts the out-of-plane information, it can not be used to remove large particle clumps. Instead, images containing large particle clumps were excluded during PIV processing by checking the number of saturated pixels. Background subtraction to remove dark-current noise was performed using the average of the remaining images. Approximately 1,000 clean preprocessed image pairs were processed by correlation ensemble averaging (or correlation averaging) using image templates of 257×129 pixels. Finally, nonlinear least square optimization was performed on the volumetric auto- and cross-correlation peaks to produce concentration and velocity measurement results.

To generate calibration data, a drop of the particle suspension used to make the flow solution was spread between two thin coverslips. The particle spread was scanned at 10 μm step in the z direction, from −250 to 250 μm about the focal plane. At each z location, 9 images of 1,024 × 1,024 pixels were captured at different x and y locations. The images at each z location were processed by ensemble-average correlation to produce a single auto-correlation peak. As the auto-correlation signal of images taken far from focal plane is low and noisy, a large number of images are used at these locations to improve the correlation signal-to-noise ratio. To generate an array of auto-correlation peaks at 1 μm steps in the z direction, cubic interpolation of the previous peaks was employed. The variations of the intensity and the width of interpolated peaks were smooth and realistic throughout the region used by the measurement algorithm.

A significant radial optical aberration was found to render the optimization unsuccessful when using $J(0,z)$ and $\sigma_{peak}(z)$ in Eqs. 5 and 10 to quickly generate the decomposed correlations. The calibration auto-correlation peaks with aberration are shown in Fig. 12. Therefore, calibration auto-correlation peaks were used directly to generate
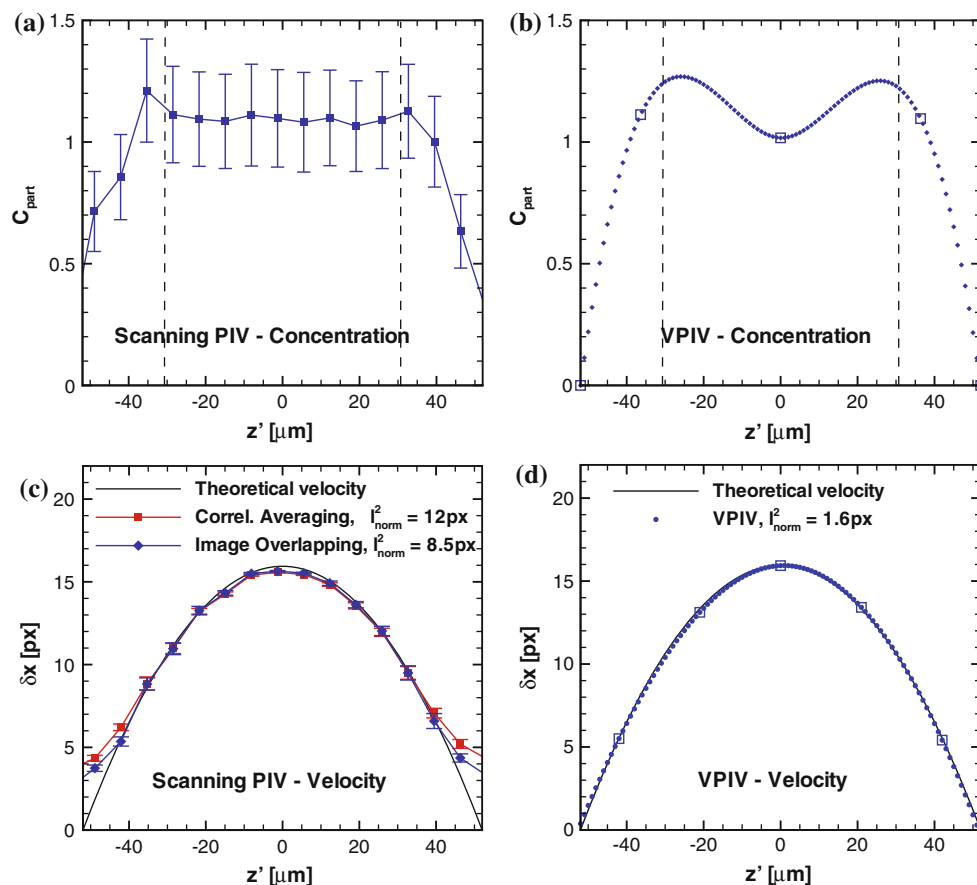

Fig. 13 Concentration and velocity measurements at the mid-plane of channel ($y = 0$) by scanning PIV (*left*) and VPIV (*right*). *Error bars* represent the standard deviation of the measurements along the channel center. The *solid curve* is the theoretical Poiseuille velocity profile calculated from the flow rate and the channel cross-section. **a** The measurement by scanning PIV overestimates the concentration at the wall. **b** Concentration measurement by VPIV displaying good accuracy everywhere including near the walls. **c** Velocity measurements both using scanning PIV with correlation averaging shown as *square*, and image overlapping shown as *diamond*, overestimate velocities near wall. **d** VPIV velocity measurement using measured concentration shown as *circle* agrees very well with theoretical profile. The *squares* are the spline nodes of the measured velocities. Both of the techniques produce maximum concentration at approximately 2/3 of the half channel depth (marked with *dashed lines*) from the flow center

$Co_{2D}(z)$ and $Cx_{2D}(\delta x, \delta y, z)$, thus overcoming the problems generated by the optical aberration. To improve the speed and the accuracy of the particle concentration and velocity measurements, the peak fitting was confined to a small area containing the peak. Concentration and velocity were iteratively obtained from the auto- and cross-correlations.
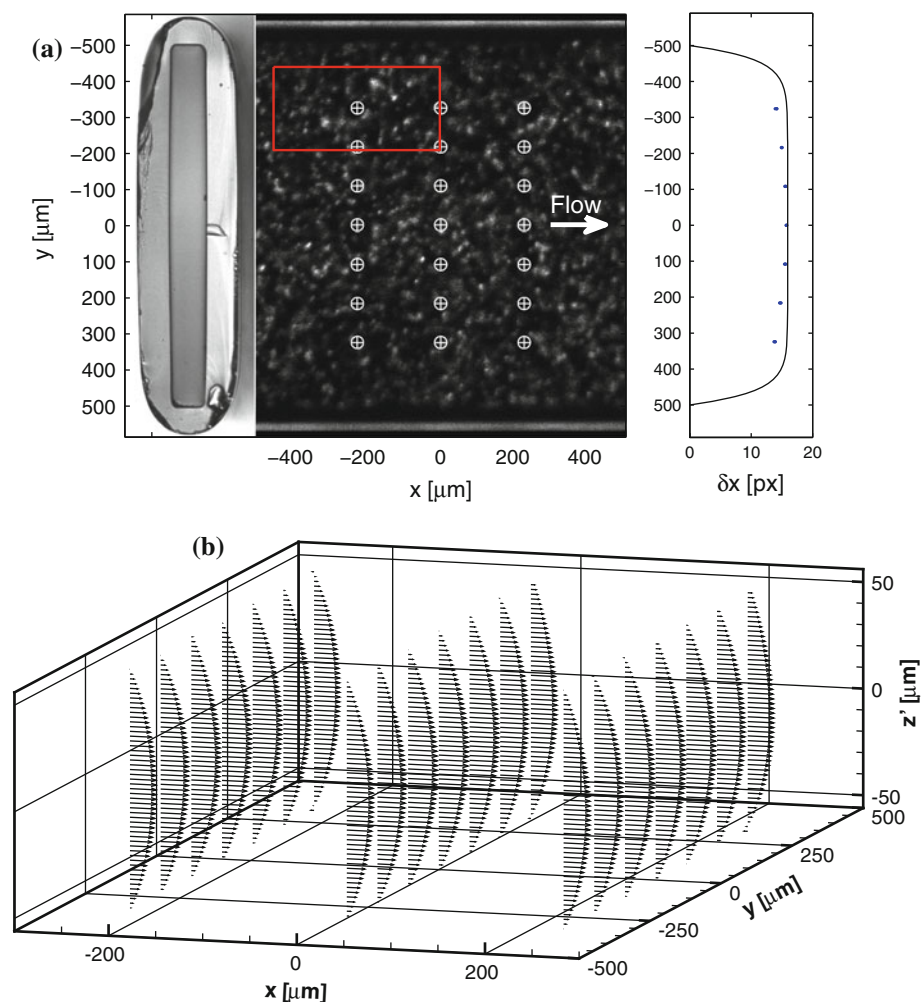
The concentration at the center of the channel is shown in Fig. 13b. As there is no theoretical concentration to compare with, it is difficult to quantitatively compare the accuracy of the concentration obtained using VPIV with that obtained using the scanning method. However, in the near-wall region, VPIV provides a realistic zero concentration at the wall while scanning technique clearly overestimates concentration in this region. On the other hand, both of the techniques produce maximum concentration at approximately 2/3 of the half channel depth (marked with dashed lines in Fig. 13) from the flow center, agreeing with the finding of Cao and Wereley (2006).

Figure 13d shows the velocity measurements versus theoretical profile calculated from the flow rate and channel cross-section (White 1991). For comparison, the velocity measurement was performed using both the measured concentration or a constant concentration assumption. As expected, the velocity measurement using measured concentration gave significantly better accuracy, $l^2_{norm} = 1.6$ px, than using constant concentration, $l^2_{norm} = 35$ px (not shown here). The excellent accuracy obtained with the improved VPIV technique is significantly better than the result using optimized scanning PIV. The greatest improvements in accuracy are in the near-wall regions where VPIV provides concentration and velocity measurements with an accuracy which is unachievable with standard micro-PIV measurements.

Finally, a 3D velocity field was obtained from using VPIV at multiple locations as shown in Fig. 14. Figure 14a shows the channel cross-section on the left, aligned with a particle image in the middle and the span-wise velocity profile on the right. Due to the change in the glass thickness near the side walls, the image region could contain some degree of distortion. VPIV measurements were performed at the locations marked with ⊕ with 50% template

Fig. 14 3D velocity measurement by VPIV from a single image plane of a single camera looking in the z direction. **a** Cross-section of the channel (*left*), the image region (*middle*) where velocity vectors were calculated at ⊕ symbols, and the velocity measured at these locations (*right*) with respect to theoretical velocity profile across the channel. The rectangle shows the size of PIV interrogation windows with 50% overlapping. The measured velocity is slightly smaller, up to 2 pixels, than the theoretical value which can be attributed to the smaller channel height towards the side walls. **b** Volumetric flow field in 3D view ($z' = z - z_0 - H/2$) where every second vector is skipped in the z direction. In the central plane ($y = 0$) parabolic profiles are clearly evident

overlapping. The rectangle shows the size of the interrogation window relative to the size of the image. VPIV measurements at the grid points produce the span-wise mid-plane velocity profile on the right of Fig. 14a where the measured velocity (dots) is slightly lower than the theoretical velocity (solid line) near the side walls, possibly due to the smaller channel height. The measurements also produce the 3D velocity field as shown in Fig. 14b. VPIV successfully produced a 3D flow field from a single image plane from a single camera using images of highly seeded flow. As expected, we see modest variations of the parabolic profiles across the width of the channel, reducing toward walls at $y = \pm 500\ \mu m$.

6 Conclusions

An enhanced volumetric-correlation particle image velocimetry (VPIV) technique providing measurement of both the 3-dimensional 2-component velocity field and corresponding out-of-plane concentration profiles is developed and demonstrated with synthetic and laboratory data. The measurements are obtained from a single image plane of a single camera in highly seeded microflows. The suitability of this technique to highly seeded flows, where tomographic PIV, holographic PTV and 3D PTV cannot be used, provides significant improvement in the information density while simultaneously allowing VPIV to be applied to a wide range of industrial and medical flows.

VPIV significantly simplifies volumetric velocity measurement by using a single camera without the need for depth scanning or particle tracking and can also be applied to time-varying flows. In addition to the cost saving of using only a single camera, the technique is suited to lower magnification, lower numerical aperture lenses, which are not only cheaper but provide a greater measurement region.

The measurement accuracy of VPIV is weakly affected by out-of-plane velocity components, but can be significantly affected by in-plane velocity gradients. The error due to in-plane gradients can be minimized by window size optimization. Future development of VPIV can incorporate in-plane velocity gradients to improve the measurement accuracy and increase the measurement capability.

VPIV provides, for the first time, an out-of-plane concentration profile measurement from a single image plane. Validation of the technique using synthetic data shows that the accuracy is comparable to that obtained using scanning techniques. Critically, the concentration information also improves the accuracy of the out-of-plane velocity measurements, providing velocity measurements which are significantly more accurate than those obtained using standard micro-PIV techniques. The improvement in measurement accuracy is especially pronounced in near-wall regions. Thus, VPIV is well suited to biological flows, such as blood flows where there are pronounced variations in blood cell concentration and of particular interest is blood cell interaction with the vessel wall.

References

Adrian R, Yao C (1985) Pulsed laser technique application to liquid and gaseous flows and the scattering power of seed materials. Appl Optics 24:42–52

Adrian R (1991) Particle-imaging techniques for experimental fluid mechanics. Annu Rev Fluid Mech Annu Rev 23:261–304

Adrian RJ (2005) Twenty years of particle image velocimetry. Exp Fluids 39:159–169

Arroyo M, Greated C (1991) Stereoscopic particle image velocimetry. Meas Sci Technol 2:1181–1186

Barnhart D, Adrian R, Papen G (1994) Phase-conjugate holographic system for high-resolution particle image velocimetry. Appl Opt 33:7159–7170

Bitsch L, Olesen L, Westergaard C, Bruus H, Klank H, Kutter J (2005) Micro particle-image velocimetry of bead suspensions and blood flows. Exp Fluids 39:507–513

Bourdon CJ, Olsen MG, Gorby AD (2004) Power filter technique for modifying depth of correlation in microPIV experiments. Exp Fluids 37:263–271

Bown M, MacInnes J, Allen R, Zimmerman W (2006) Three-dimensional, three-component velocity measurements using stereoscopic micro-PIV and PTV. Meas Sci Technol 17:2175–2185

Chamarthy P, Garimella S, Wereley S (2009) Non-intrusive temperature measurement using microscale visualization techniques. Exp Fluids 47:159–170

Cao J, Wereley ST (2006) Micro-particle image velocimetry in biomedical applications. In: Bowlin GL, Wnek G (eds) Encyclopedia of biomaterials and biomedical engineering.. Informa Healthcare, New York, pp 1873–1884

Cummings EB (2000) An image processing and optimal nonlinear filtering technique for particle image velocimetry of microflows. Exp Fluids 29:S42–S50

Elsinga G, Scarano F, Wieneke B, van Oudheusen B (2006) Tomographic particle image velocimetry. Exp Fluid 41:933–947

Erkan N, Shinohara K, Someya S, Okamoto K (2008) Three-component velocity measurement in microscale flows using time-resolved PIV. Meas Sci Technol 19:057003

Fouras A, Dusting J, Lewis R, Hourigan K (2007) Three-dimensional synchrotron X-ray particle image velocimetry. J Appl Phys 102:064916:1–6

Fouras A, Lo Jacono D, Hourigan K (2008) Target-free stereo PIV: A novel technique with inherent error estimation and improved accuracy. Exp Fluids 44(2):317–329

Fouras A, Lo Jacono D, Nguyen CV, Hourigan K (2009) Volumetric correlation PIV: a new technique for 3D velocity vector field measurement. Exp Fluids 47(4):569–577

Grothe R, Dabiri D (2008) An improved three-dimensional characterization of defocusing digital particle image velocimetry. Meas Sci Technol 19:065402

Gui L, Wereley ST, Lee SY (2002) Digital filters for reducing background noise in micro PIV measurement. In 11th international symposium on the application of laser techniques to fluid mechanics, Lisbon

Huang HT, Fiedler HE, Wang JJ (1993) Limitation and improvement of PIV, part I: limitation of conventional techniques due to deformation of particle image patterns. Exp Fluids 15:168–174

Kahler C (2004) Investigation of spatio-temporal flow structure in the buffer region of a turbulent boundary layer by means of multiplane stereo PIV. Exp Fluid 36:114–130

Kajitani L, Dabiri D (2005) A full three-dimensional characterization of defocusing digital particle image velocimetry. Meas Sci Technol 16:790–804

Keane RD, Adrian RJ (1992) Theory of cross-correlation analysis of PIV images. Appl Sci Res 49(3):191–215

Lindken R, Westerweel J, Wieneke B (2006) Stereoscopic micro particle image velocimetry. Exp Fluids 41:161–171

Meinhart CD, Wereley ST, Gray MHB (2000) Volume illumination for two-dimensional particle image velocimetry. Meas Sci Technol 11:809–814

Meinhart CD, Wereley ST, Santiago JG (2000) A PIV algorithm for estimating time-averaged velocity fields. J Fluids Eng 122:285–289

Nesbitt W, Westein E, Tovar-Lopez F, Tolouei E, Mitchell A, Fu J, Carberry J, Fouras A, Jackson SA (2009) Shear gradient-dependent platelet aggregation mechanism drives thrombus formation. Nat Med 15:665–673

Nguyen CV, Fouras A, Carberry J (2010) Improved accuracy of micro PIV measurement using image overlapping technique. Exp Fluid 49(3):701–712

Olsen MG, Adrian RJ (2000) Out-of-focus effects on particle image visibility and correlation in microscopic particle image velocimetry. Exp Fluids 29(7):S166–S174

Olsen MG, Adrian RJ (2000) Brownian motion and correlation in particle image velocimetry. Opt Laser Technol 32:621–627

Olsen MG, Bourdon CJ (2003) Out-of-plane motion effects in microscopic particle image velocimetry. J Fluids Eng 125:895–901

Park J, Kihm K (2006) Three-dimensional micro-PTV using deconvolution microscopy. Exp Fluid 40:491–499

Pereira F, Gharib M, Dabiri D, Modarress M (2000) Defocusing DPIV: a 3-component 3-D DPIV measurement technique application to bubbly flows. Exp Fluid 29:S78–S84

Pereira F, Gharib M (2002) Defocusing digital particle image velocimetry and the three-dimensional characterization of two-phase flows. Meas Sci Technol 13:683–694

Pereira F, Lu J, Castaño-Graff E, Gharib M (2007) Microscale 3D flow mapping with µDDPIV. Exp Fluids 42:589–599

Plecis A, Malaquin L, Chen YA (2008) A method for fast monitoring of flow rates in microfluidic channels. J Appl Phys 104:124909

Poelma C, Westerweel J (2010) Generalized displacement estimation for averages of non-stationary flows. Exp Fluids. Online. doi: 10.1007/s00348-010-1002-1

Santiago J, Wereley S, Meinhart C, Beebe D, Adrian RA (1998) Particle image velocimetry system for microfluidics. Exp Fluids 25:316–319

Satake S, Kunugi T, Sato K, Ito T, Kanamori H, Taniguchi J (2006) Measurements of 3D flow in a micro-pipe via micro digital holographic particle tracking velocimetry. Meas Sci Technol 17:1647–1651

Schroder A, Kompenhans J (2004) Investigation of a turbulent spot using multi-plane stereo particle image velocimetry. Exp Fluids 36:82–90

Sheng J, Malkiel E, Katz J (2006) Digital holographic microscope for measuring three-dimensional particle distributions and motions. Appl Opt 45:3893–3901

Tangelder G, Slaaf D, Muijtjens A, Arts T, oude Egbrink M, Reneman R (1986) Velocity profiles of blood platelets and red blood cells flowing in arterioles of the rabbit mesentery. Circ Res Am Heart Assoc 59:505–514

Wereley ST, Gui L, Meinhart CD (2002) Advanced algorithms for microscale particle image velocimetry. AIAA J 40:1047–1055

White FM (1991) Viscous fluid flow. 2nd edn. McGraw-Hill Book Company, Singapore, pp 114–121

Willert C, Gharib M (1992) Three-dimensional particle imaging with a single camera. Exp Fluid 12:353–358

Yoda M, Sadr R (2004) Nano-particle image velocimetry (nPIV): a new technique for measuring near-wall velocity fields with submicron spatial resolution. AIAA paper 8686–8693

Yoon S, Kim K (2006) 3D particle position and 3D velocity field measurement in a microvolume via the defocusing concept. Meas Sci Technol 17:2897–2905

Zhang J, Tao B, Katz J (1997) Turbulent flow measurement in a square duct with hybrid holographic PIV. Exp Fluid 23:373–381

Zheng X, Silber-Li Z (2008) Measurement of velocity profiles in a rectangular microchannel with aspect ratio $\alpha = 0.35$. Exp Fluids 44:951–959